

2008-03-04

# Segmentation of Patient-Specific 3D Cardiac Magnetic Resonance Images of Human Right Ventricle

Xueying Huang  
*Worcester Polytechnic Institute*

Follow this and additional works at: <https://digitalcommons.wpi.edu/etd-dissertations>

---

## Repository Citation

Huang, X. (2008). *Segmentation of Patient-Specific 3D Cardiac Magnetic Resonance Images of Human Right Ventricle*. Retrieved from <https://digitalcommons.wpi.edu/etd-dissertations/65>

This dissertation is brought to you for free and open access by [Digital WPI](#). It has been accepted for inclusion in Doctoral Dissertations (All Dissertations, All Years) by an authorized administrator of Digital WPI. For more information, please contact [wpi-etd@wpi.edu](mailto:wpi-etd@wpi.edu).

**Segmentation of Patient-Specific 3D Cardiac Magnetic  
Resonance Images of Human Right Ventricle**

A Project Report

Submitted to the Faculty

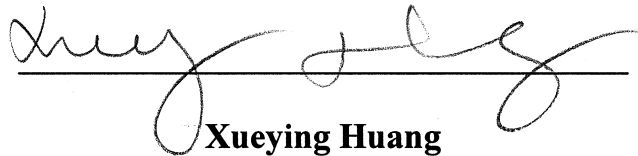
of the

WORCESTER POLYTECHNIC INSTITUTE

in Partial Fulfillment of the Requirements of the

Degree of Doctor of Philosophy

by

  
\_\_\_\_\_

**Xueying Huang**

Date: February 28, 2008

Approved by,

  
\_\_\_\_\_

**Professor: Dalin Tang, Advisor**

  
\_\_\_\_\_

**Professor: Tal Geva, MD, Co-Advisor**

  
\_\_\_\_\_

**Professor: Andrew J. Powell, MD, Co-Advisor**

## **ABSTRACT**

Right Ventricular (RV) dysfunction is a common cause of heart failure in patients with congenital heart defects and often leads to impaired functional capacity and premature death. 3D cardiac magnetic resonance imaging (CMR)-based RV/LV combination models with fluid-structure interactions have been introduced to perform mechanical analysis and optimize RV remodeling surgery. Obtaining accurate RV/LV morphology is a very important step in the model-constructing process. A semi-automatic segmentation process was introduced in this project to obtain RV/LV/Valve geometry from patient-specific 3D CMR images. A total of 420 contour results were obtained from one patient CMRI data using QMASS software package at Department of Cardiology of Children's hospital. The digital contour data were automatically acquired using a self-developed program written in MATLAB. 3D visualizations of the RV/LV combination model at different phases throughout the cardiac cycle were presented and RV/LV volume curves were given showing the volume variation based on digital contour data under MATLAB environment. For the patient considered, the RV stroke volume (SV) is 190.8 ml (normal value is 60-136 ml) and ejection fraction is 43.5% (normal value is 47%-63%). In future work, the surgical, CMR imaging and computational modeling will be integrated together to optimize patch design and RV volume reduction surgery procedures to maximize recovery of RV cardiac function.

## **ACKNOWLEDGEMENT**

I would like to express my deepest gratitude to Professor Dalin Tang, my advisor, for his tremendous help, constant encouragement, patient guidance, and thoughtful advice during my project and my study at Worcester Polytechnic Institute. Without his help and support, this project would never have been completed. I would also like to sincerely thank Professor Tal Geva (Children's Hospital, Boston), co-advisor of my project, for his valuable guidance, help and encouragement and providing me the opportunity to do the segmentation work in the Department of Cardiology at Children's Hospital Boston. His numerous suggestions and support have made my project possible. I would like to thank Professor Andrew J. Powell (Children's Hospital, Boston), co-advisor of my project, for his great help and guidance. I am especially thankful to Dr. Rebecca Beroukhim (Children's Hospital, Boston) who gave me the first training with the numerous patience, help, and encouragement. Finally, I would also like to thank my parents for their constant love and emotional support during my studies here.

# TABLES OF CONTENTS

<b>ABSTRACT.....</b>	<b>2</b>
<b>ACKNOWLEDGEMENT.....</b>	<b>3</b>
<b>TABLES OF CONTENTS.....</b>	<b>4</b>
<b>LIST OF FIGURES .....</b>	<b>6</b>
<b>LIST OF TABLES.....</b>	<b>9</b>
<b>1. INTRODUCTION.....</b>	<b>10</b>
<b>2. BACKGROUND.....</b>	<b>12</b>
2.1 Description of the Clinical Problem.....	12
2.2 Mechanism of RV Dysfunction in Repaired ToF patients.....	13
2.3 Current Management of Failing RV in ToF Patients.....	14
2.4 Novel Clinical Trials and Modelling Approaches.....	16
<b>3. CMRI DATA ACQUISITION.....</b>	<b>18</b>
<b>4. SEGMENTATION.....</b>	<b>19</b>
4.1 Segmentation for CMRI.....	20
4.1.1 QMASS MR Workspace Window.....	20
4.1.2 Creating Contours.....	21
4.1.3 Editing/ Examining the Contour.....	23

4.2 Saving the Digital Contour Results.....	27
4.2.1 Using PrintScreen to Save Contour Results.....	27
4.2.2 Obtaining Data of Digital Contours Using MATLAB.....	28
<b>5. RESULTS AND ANALYSIS.....</b>	<b>32</b>
5.1 Segmentation Results.....	32
5.2 Computing Area and Volume.....	34
5.3 Ventricle Function Analysis.....	36
<b>6. FUTURE WORK: MODELING FOR SURGERY OPTIMIZATION.....</b>	<b>38</b>
6.1 3D MRI Based Computational Models.....	38
6.1.1 Solid and Flow Model.....	38
6.1.2 Solution Procedures.....	42
6.2 Baseline Results from the RV/LV FSI Model for a Normal Healthy RV.....	42
6.3 RV Model Development for Surgery Optimization.....	45
<b>7. CONCLUSIONS AND DISCUSSION .....</b>	<b>47</b>
<b>REFERENCES.....</b>	<b>49</b>

## LIST OF FIGURES

**Figure 1.** Diagrams showing tetralogy of Fallot (ToF) and repaired ToF heart. (a) ToF heart, in which both the aorta (AO) and the pulmonary artery (PA) are connected to the right ventricle (RV); (b) ToF after surgical repair: The ventricular septal defect is patched to prevent right-to-left shunt; RV outflow tract is widened to increase blood flow to lungs.

**Figure 2.** Repaired tetralogy of Fallot (ToF) heart with RV outflow patch and scar [4]. (a) ToF heart with RV outflow patch and scar on anterior RV wall, large shaded area indicates area of akinesis/dyskinesis; (b) Current management: Heart after pulmonary valve insertion (PVR) and reduction of RV outflow patch; (c) Novel clinical trial (surgical RV remodeling): PVR, reduction of RV outflow patch and removal of RV scar.

**Figure 3.** 3D End-diastolic and End-systolic CMR images acquired from the patient

**Figure 4.** Main workspace window consists of a menu bar, a tool bar and a study view, active image view, thumbnail View.

**Figure 5.** Procedure of detecting the contours using point mode. a) Place points on the contour; b) Generate the contour.

**Figure 6.** CMR Images of S12P29: a) Original CMR Image; b) Incorrect segmentation results; c) Correct segmentation results.

**Figure 7.** CMR Images of slice 12 for all phases (Time 1 - Time 30) in a cardiac cycle.

**Figure 8.** Image presents on the screen (showing results of S9P29) is saved using Print Screen key.

**Figure 9.** Images of selected region of S9P29. (a) The region of S9P29 which is parallel to original CMRI Image with contour results; (b) Shows original RGB images of interested (show the region of RV/LV to for better presentation); (c) Red component image showing different value of the 4 different contours.

**Figure 10.** Chain code, 0-7 represents 8 directions of the center point [23].

**Figure 11.** CMR Images with segmented RV/LV contours (End of Diastole) acquired from a patient showing the RV/LV morphologies

**Figure 12.** Plots showing the 3D-reconstructed model based on segmented result. (a) A health human heart sketch showing left and right ventricles with valve position; (b) Segmented RV/LV MRI contour plots; (c) The re-constructed 3D geometry of the RV/LV combination model; (d) The 3D reconstructed model with outer boundary at End of Diastole (left) and End of Systole (right) showing the heart contraction/expansion.

**Figure 13.** Patient-specific RV/LV volume curves showing the RV/LV volume variety.

**Figure 14.** Experimental data for RV material properties and the stress-stretch curve derived from the Mooney-Rivlin model with parameters selected to fit experimental data. Parameter values used for the MR model:  $c_1 = 3600 \text{ dyn / cm}^2$ ,  $D_1 = 818 \text{ dyn / cm}^2$ ,  $c_2 = 0$ ,  $D_2 = 12$  [11].

**Figure 15.** Recorded and prescribed pressure conditions at the tricuspid (inlet) valve (TV) and pulmonary (outlet) valve (PV) [15]. Prescribed numerical pressure conditions and valve close/open times were modified from the recorded data so that pressure conditions were as consistent with the recorded data as possible. The vertical bars in (c) indicate valve open/close switch time.



**Figure 16.** Position of the cut-surface selected for presentation of 3D results.

**Figure 17.** Velocity plots at different phases showing interesting flow patterns. a) Beginning of the filling phase; b) Flow patterns just before the end of filling phase; c) Beginning of the ejection. The inlet just closed and the outlet valve is open. d) Ejection continues.

**Figure 18.** Maximal principal stress/strain (Stress-P1 and Strain-P1) distributions on the RV inner surface may provide useful information for mechanical analysis and disease assessment. a) Stress-P1 on the inner surface of RV portion given by Fig. 16(b) under maximum pressure; b) Strain-P1 on the inner surface of RV under maximum pressure; c)-d) Stress/Strain plots corresponding to minimum pressure condition. Figures were flipped 180° horizontally to have the same view as velocity figures.

## LIST OF TABLE

**Table 1.** Buttons in the Element section of the toolbar used for creating contour.

**Table 2.** Contour shape tools for contours refine.

**Table 3.** Patient-specific End of Diastolic and Systolic RV/LV volume data.

**Table 4.** Summary of RV volume and normal range comparison results.

**Diagram 1.** A flowchart showing the model development and validation process.

# 1. INTRODUCTION

Three-dimensional (3D) patient-specific cardiac magnetic resonance (CMR) image-based computational models for the right ventricle (RV) with fluid-structure interactions (FSI) have been introduced to perform mechanical analysis, provide pre- and post-operative cardiac function analysis and optimize RV remodeling surgical procedures [26-29, 38]. RV morphology is the most fundamental element needed to construct these computational models. It is well known that high resolution CMR is capable to visualize the four cardiac chambers, the two atria and the two ventricles. Accurate digital RV/LV contour data based on segmentation results of CMR images are needed to obtain the RV/LV morphology.

The objectives of this project are the following:

- 1) To apply noninvasive CMR techniques to segment patient-specific in vivo CMR Images of a human heart;
- 2) To develop a program package to automatically obtain digital RV/LV contour data based on segmentation results;
- 3) To perform initial mechanical analysis based on obtained CMR data for the construction and validation of computational ventricle models.

The effort of this project was three fold. The first was to segment CMR images of a patient with repaired tetralogy of Fallot (ToF) congenital heart disease, using QMASS software package at Children's Hospital Boston. The segmentation results were then stored to figures with .tiff image type without compression. Secondly, a Matlab-based package, Digital Contour Detecting for Heart Images (DCDHI), was developed for automatically detecting/saving the digital contours of the RV and the LV based on obtained images with segmentation results. The resulting accurate digital RV/LV contours would be used for future computational modeling.

The third was to re-construct 3D RV/LV model and perform basic volumetric analysis, such as calculate RV stroke volume (SV) and ejection fraction (EF), which are two common measures for right ventricular functions.

This project provided an opportunity for the author to learn directly from cardiologists, cardiac radiologist and other medical professionals at Children's Hospital Boston, Harvard Medical School, and get first-hand knowledge about the entire CMR data acquisition process in a true hospital setting. This is a great help for the author to better understand the biological background of heart circulation. DCDHI developed in this project will be a considerable help to obtain the digital contour of RV/LV, which is a very important modeling issue.

In the future, 3D CMR-based patient-specific RV/LV/Patch combination models with fluid-structure interactions will be developed to assess and optimize RV remodeling surgical procedures and RV outflow patch design using the digital contours obtained in this project.

## 2. BACKGROUND

### 2.1. Description of Tetralogy of Fallot

Tetralogy of Fallot (ToF) is a congenital heart malformation that comprises a ventricular septal defect, rightward malposition of the aorta, infundibular pulmonary stenosis, and right ventricular hypertrophy (Fig.1 (a)). The malformation is thought to result from underdevelopment of the subpulmonary infundibulum during early embryonic development with all elements of the anomaly resulting from this abnormality. ToF is the most common cyanotic cardiac defect, with an incidence of 3.26 per 10,000 live births, or about 1300 new cases per year in the United States [7].

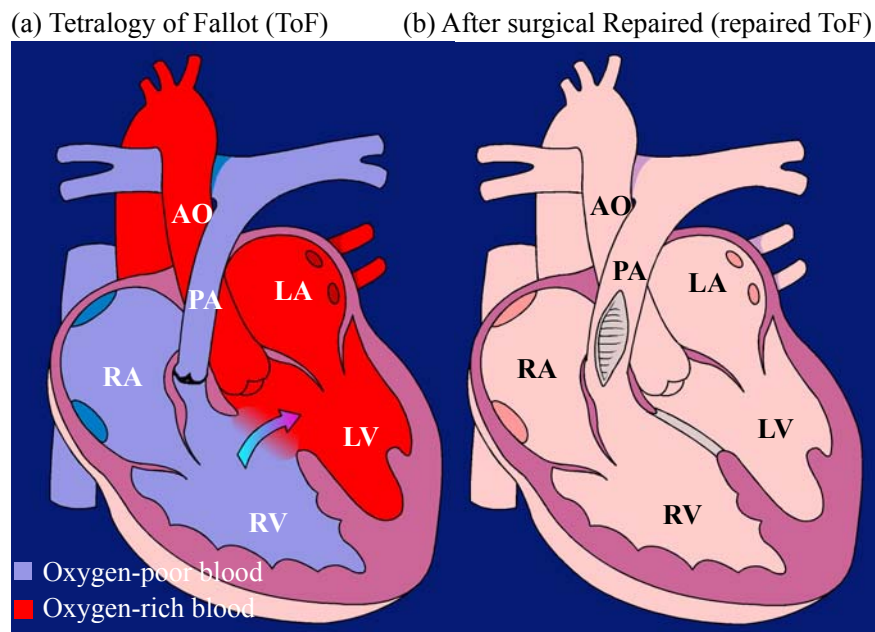


*Fig. 1. Diagrams showing tetralogy of Fallot (ToF) and repaired ToF heart. (a) ToF heart, in which both the aorta (AO) and the pulmonary artery (PA) are connected to the right ventricle (RV); (b) ToF after surgical repair: The ventricular septal defect is patched to prevent right-to-left shunt; RV outflow tract is widened to increase blood flow to lungs.*

The anomaly begins during early embryonic development with a narrowed pulmonary valve and a defect between the ventricles (called ventricular septal defect or VSD). The defect is tolerated well by the fetus because only a small amount of blood flows through the lungs until birth. After birth, the blood that is supposed to start flowing through the lungs cannot easily get there due to the narrowed right ventricular outflow tract and pulmonary valve; however, the ventricular septal defect remains open so that much of the blood that comes back to the heart needing oxygen is sent out without being properly oxygenated. In addition, the right ventricle (RV) has to pump at the same pressure as the left ventricle (LV). Several changes follow. First, the baby turns cyanotic because the deoxygenated blood that bypasses the lungs mixes with the oxygenated blood and lowers the oxygen saturation of the systemic blood. Deoxygenated blood is darker and appears blue through the skin. Second, the right ventricle hypertrophies from the increased pressure load imposed on it. Next, the low oxygen saturation of the systemic blood causes it to get thicker and clot more easily. Clots in the veins can now pass through the ventricular septal defect and directly enter the aorta, where they can do much more damage than in the lungs—such as causing infarcts in the brain [13].

Survival of patients with ToF past the first two decades of life has improved with recent reports showing a 20-year survival rate nearing 90% since surgical repair of ToF (Fig.1 (b)) has been performed successfully over the last 45 years [17, 19]. However, in long-term follows up, considerable and rising late morbidity and mortality are encountered which is related to right ventricular (RV) dysfunction/dilatation and heart failure.

## **2.2. Mechanism of RV Dysfunction in Repaired ToF patients**

After surgical repair of ToF, most patients have an excellent functional result and lead a

normal active and social life. Nevertheless, surgical repair of ToF usually comprises incision into the right ventricular outflow tract (RVOT), removal of obstructive cardiac muscle, removal of obstructive pulmonary valve tissue, and placement of a patch made of non-contracting tissue or synthetic material to widen the RVOT and pulmonary valve annulus. Consequently, the majority of these patients have residual hemodynamic abnormalities, primarily due to chronic pulmonary regurgitation (PR) that leads to RV volume overload. Additional hemodynamic abnormalities such as residual RVOT obstruction, branch pulmonary artery stenosis, tricuspid regurgitation, or a residual ventricular septal defect can further aggravate right and/or left ventricular dysfunction [22]. Thus, although early results with surgical repair of ToF are very good, late results are not as good and many if not most of these patients develop progressive right ventricular dilatation and dysfunction over time. Paradoxically, due to the improved survival with surgery for ToF in infancy achieved in the 80s, the number of ToF patients presenting in their third and fourth decade of life with severe RV dilation and dysfunction is growing rapidly.

### **2.3. Current Management of Failing RV in ToF patients**

The surgical treatment of patient with repaired ToF presenting with RV dysfunction traditionally has been to eliminate the defects that directly impact on RV volume with the thought that RV dilatation per se, is the cause of RV dysfunction. Thus, much of the emphasis has centered on elimination of pulmonary regurgitation by replacing/inserting a prosthetic pulmonary valve, and reduction of the RV outflow patch (Fig. 2 (b)).

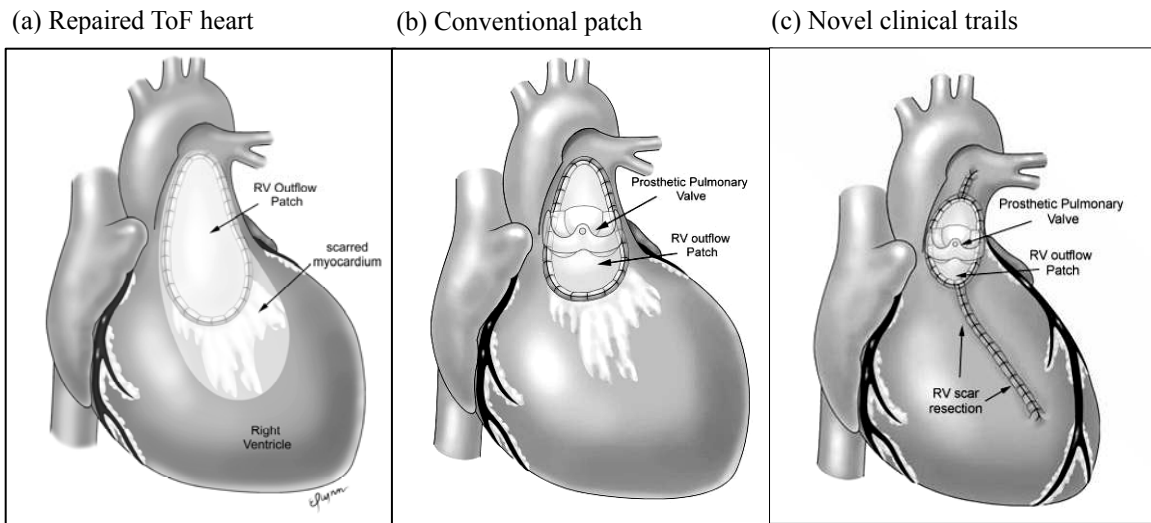


*Fig. 2. Repaired tetralogy of Fallot (ToF) heart with RV outflow patch and scar [4]. (a) ToF heart with RV outflow patch and scar on anterior RV wall, large shaded area indicates area of akinesis/dyskinesis; (b) Current management: Heart after pulmonary valve insertion (PVR) and reduction of RV outflow patch; (c) Novel clinical trial (surgical RV remodeling): PVR, reduction of RV outflow patch and removal of RV scar.*

Studies evaluating the results of this approach indicate that in most patients there is a significant decrease in RV end-diastolic volume [37], which is the index used to assess volume load of the ventricle. However more recent studies focusing on RV function after surgery have found mixed results. Some clinical reports indicate that the surgical treatments result in decrease in RV volume and some improvement in RV function, while in others showing no significant improvement in RV function after surgery. The differences in these findings may relate to methodology such as use of magnetic resonance imaging (MRI) in the latter studies, but likely also indicate that there is significant heterogeneity in this patient population. There are some reports indicate that the worse systolic function pre-operatively in the latter group may have contributed to the lack of improvement in RV function with pulmonary valve



replacement/insertion (PVR) alone. The lack of predictable improvement in ejection fraction after PVR alone is of concern, and suggests that persistent RV dysfunction is a marker of adverse remodeling with scar formation and fibrosis, and that conventional procedures with PVR alone are not enough for many patients.

#### **2.4. Novel Clinical Trial and Modeling Approaches to Treat RV Dysfunction in ToF**

Dr. del Nido and Dr. Geva developed a novel surgical technique for achieving direct volume reduction of the right ventricle by removing the scarred myocardium from the RV outflow and adjacent anterior wall of the RV (Fig. 2 (c)). This procedure, which is named surgical RV remodeling, aims to reduce the RV volume and remove the non- or poorly contractile tissue in the RV.

Computational modeling and medical imaging technologies have made considerable advances in biological and clinical research in recent years [34, 35] and in particular noninvasive cardiac magnetic resonance (CMR) has enabled to quantify the geometry, blood flow in any desired location. However, three-dimensional patient-specific MRI-based models of the RV with fluid-structure interaction (FSI), can provide pre- and post-operative RV cardiac function analysis and optimize RV remodeling surgical procedures, are still lacking in the literature and clinical practice.

Prof. Tang, Dr. del Nido and Dr. Tal Geva et al. introduced an interdisciplinary procedure integrating surgical RV remodeling, non-invasive CMR imaging technology, and 3D CMR-based patient-specific computational modeling to analyze RV flow and structure, stress/strain distributions, and assess RV cardiac function for optimal surgery design [26, 30, 38]. This procedure will address not only on pulmonary valve regurgitation for RV dysfunction and

dilation but also address mechanical properties. This research may benefit a growing population of patients with repaired ToF.

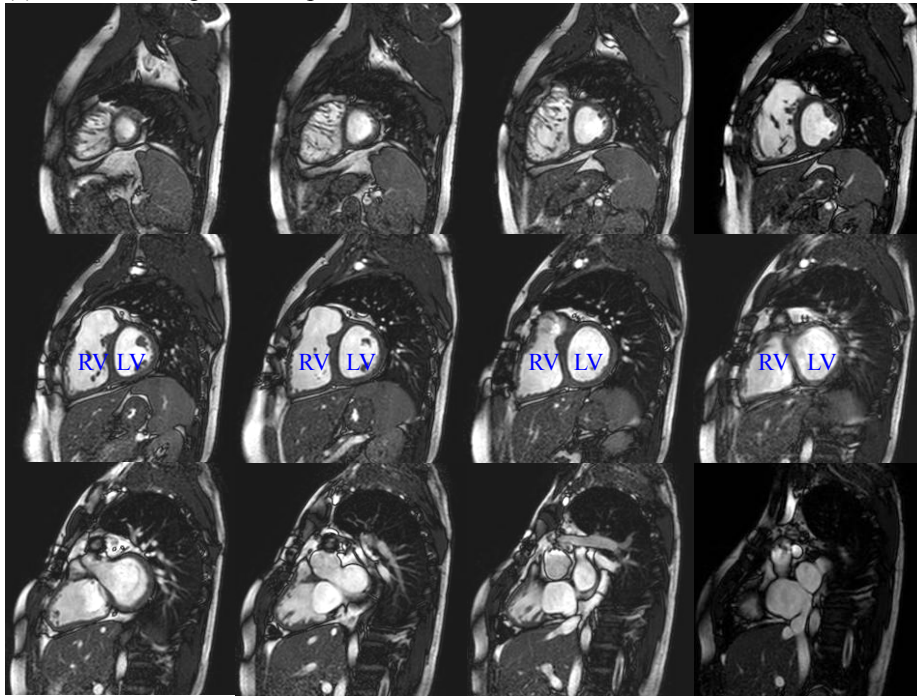
### 3. CMRI DATA ACQUISITION

Cardiovascular magnetic resonance (CMR) is established in clinical practice for the diagnosis and management of congenital and acquired heart diseases [7, 9]. In contrast to 2-D echocardiography, angiocardiography, and radionuclide techniques, CMR does not rely on geometrical assumptions, is accurate regardless of the shape or orientation of the chamber, and most investigators now consider it the gold standard imaging modality for assessment of ventricular dimensions and function [12, 16, 18, 20]. Noninvasive CMR techniques have enabled to quantify the geometry, blood flow in any desired location, including quantification of pulmonary regurgitation and measure biventricular systolic function [21, 36].

The original CMRI data were provided by Department of Cardiology of Children's Hospital Boston. Cardiac MRI studies were performed using a dedicated MRI suite located in Department of Cardiology of Children's Hospital Boston. The unit employs a 1.5 Tesla Philips Achieva scanner equipped with a Nova dual gradients system with maximal amplitude of 66 mT/m and a maximal slew rate of 160T/m/s (Philips Medical Systems, Best, The Netherlands). This state-of-the-art scanner includes all currently available cardiac imaging sequences.

The patient, now a 23-years-old male, underwent surgical repair of ToF in infancy and has severe pulmonary valve regurgitation and RV dilatation. The image data set were assessed using an electrocardiography (ECG)-triggered steady state free precession (SSFP) cine MRI sequence. The following imaging parameters were used: echo time (TE): 1.41 ms; repetition time (TR): 2.81ms; flip angle: 60 degrees; field of view (FOV): 302 x 302 mm; image resolution: 256 x 256 pixels; slice thickness: 8 mm; inter-slice gap: 2 mm; number of reconstructed images per cardiac cycle: 30. Fig. 3 presents a set of end-diastolic/end-systolic CMR images of this patient.

(a) 3D CMR Images from a patient, End of Diastole for RV/LV



(b) 3D CMR Images from a patient, End of Systole for RV

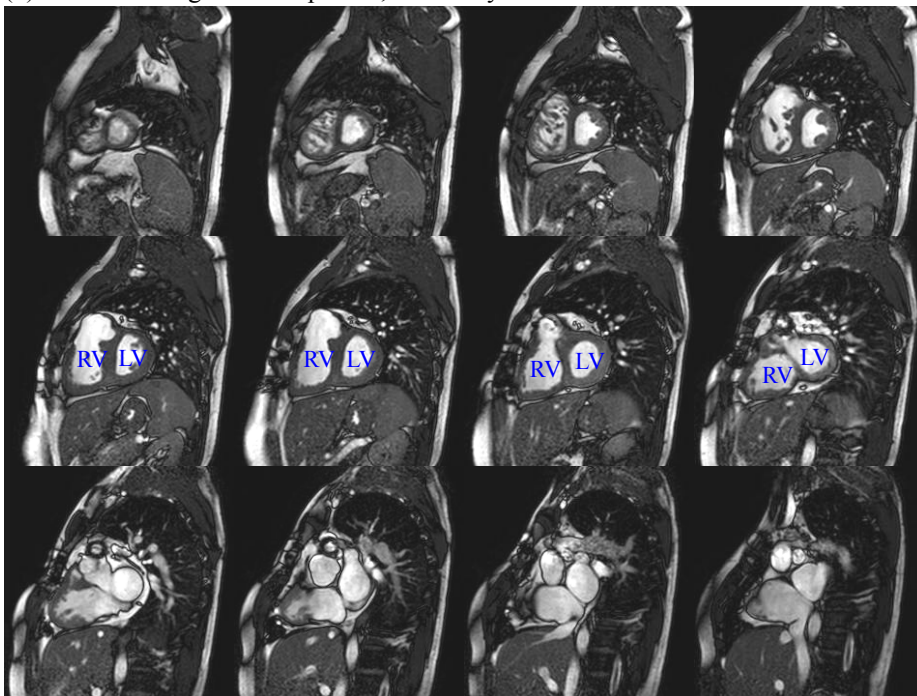


*Fig. 3. 3D End-diastolic and End-systolic CMR images acquired from the patient.*

## 4. SEGMENTATION

### 4.1. Segmentation for CMRI

CMRI data were reviewed on a ViewForum workstation (Philips Medical Systems, Best, The Netherlands). Segmentation was performed with QMASS<sup>®</sup> (MR Analytical Software, Medis Medical Imaging Systems, Leiden, The Netherlands), an analytical software system for quantitative analysis of cardiac MRI studies.

#### 4.1.1 QMASS MR Workspace Window

At the starting page of QMASS software, double-click the shortcut on the desktop or select **Start > Programs > Medis > QMASS MR** to start working with QMASS. Then click **Database > Open Study...** in the menu bar to select the study to analyze. The main workspace window consists of a menu bar, a tool bar, and three views, is given by Fig. 4.

The Study View uses a matrix to show a representation of the images in the currently loaded study. Every gray button in the matrix stands for a specific image in the study. A row and a column in the matrix represent a slice and a phase, respectively. The study view can be used to select the images to edit in the Active Image View. The Thumbnail View shows the images in the slice or phase direction that have been selected in the Study View. The currently selected image is shown with a red frame.

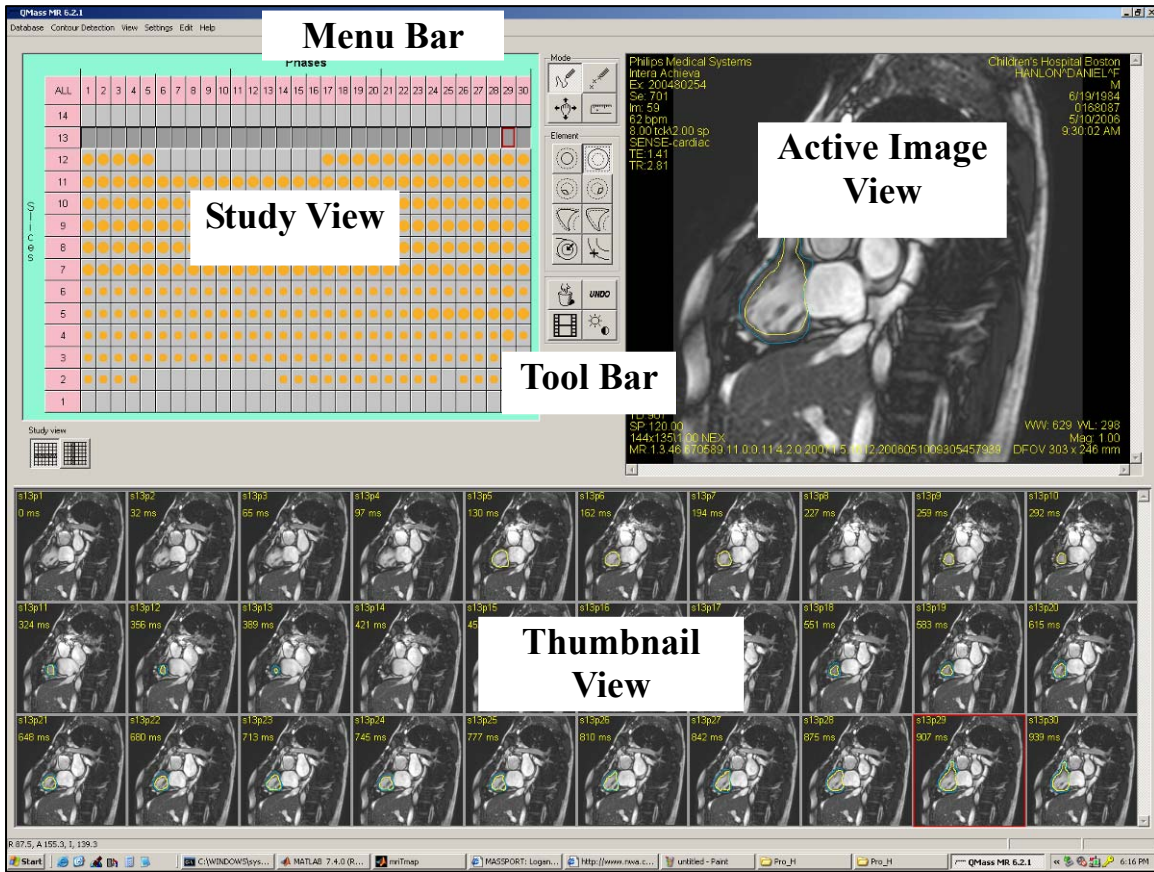


Fig. 4. Main workspace window consists of a menu bar, a tool bar and a study view, active image view, thumbnail View.

#### 4.1.2 Creating Contours

The first step of creating contours is to pick the systole (smallest) and diastole (largest) phases. The Thumbnail View could be used to show the images in the phase for each slice. Pay attention to the images which are getting bigger, then smaller or getting smaller, then getting bigger. The Movie Tool also allows us to view slices or phases of CMR as movies. This tool is of great help to find the systole and diastole phases. The diastolic phases of RV and LV are usually the same but the systolic phase may differ for the LV and the RV due to conduction delay. For this patient, the diastolic phase of RV/LV is phase 29, while the LV systolic phase is phase 11,

and RV systolic phase is phase 14.

Click Phase 29 (diastole) to do segmentation first. The following elements of toolbar (Table.1) will be used to detect the contours of LV/RV endocardial (inner boundary) and epicardial (outer boundary) contours.









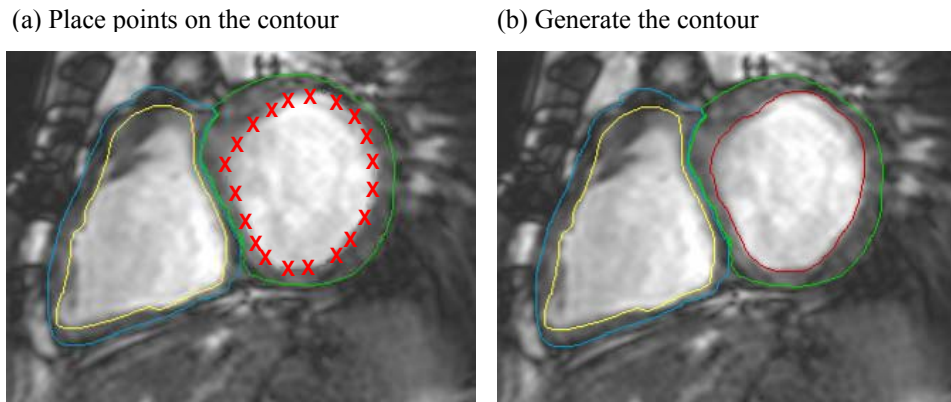

	<b>Place the points of Contour</b>		<b>Place the line of Contour</b>
	<b>Detect LV endocardial contours</b>		<b>Detect LV epicardial contours</b>
	<b>Detect RV endocardial contours</b>		<b>Detect RV epicardial contours</b>

Table 1. Buttons in the Element section of the toolbar used for creating contour.

Manually drawing contours is usually chosen to create the contours due to the image quantity and the large deformation due to heart beating (expansion and contraction). Here is an example to create contours of LV endocardial. Select  in the Element section of the toolbar to detect LV endocardial contours. There are two modes to draw the contour, one is Point Mode, and the other is Trace Mode. If using Point Mode to create the contour, first, click  in the tool bar; when moving the cursor over the Active Image View, it becomes cross-shaped. This is followed by clicking in the image to mark all the points of the contour, either in clockwise or in counter-clockwise direction (Fig. 5 (a)). Finally, after placing the last point, double click. The software will automatically draw the contour along the points that have been placed. In the Study View, a red circle appears in the images that represents the contour (Fig. 5 (b)).



*Fig. 5. Procedure of detecting the contours using point mode: a) Place points on the contour; b) Generate the contour.*

For Trace mode, click  button, then click in the image, hold down the mouse button and trace the contour. When reach the end of the contour, release the mouse, the software will automatically draw the contour. In the Study View, a red circle appears in the images that represents the image. Comparing with these two modes, Point mode creates the contour based on points placed in the image, and Trace mode creates the contour based on the contour drew.

We can click the other Detect Contour buttons, and repeat the above steps to obtain RV endocardial, and LV/RV epicardial contours. Different color circles represent different contours: green/blue and red/yellow circles represent LV/RV epicardial and LV/RV endocardial contours respectively (Fig. 5 (b)).

#### **4.1.3 Editing/Examining the Contour**

When finishing the contours, we must check the detected contours, and edit them where necessary, especially for those images including Valves. This is because the segmentation job



might not be correct if only based on the image features due to the complication of heart large deformation in a cycle especially for the slices located on the bottom and top position. The following is an example.

Fig. 6 (a) gives the original CMR images of slice 12 in phase 29. Fig. 6 (b) presents the segmentation results only based on the features of this image. However, RV endocardial and epicardial contours are not correct because the contours do not show the correct position of tricuspid valve (Fig. 6(c) shows the correct segmentation results). Therefore, the examination is needed for the accuracy of segmentation.

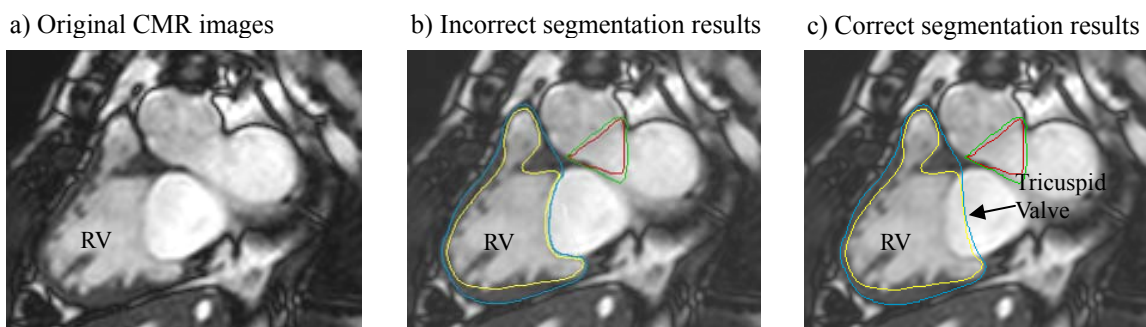


*Fig. 6. CMR Images of S12P29: a) Original CMR Image; b) Incorrect segmentation results; c) Correct segmentation results.*

Indeed, tricuspid valve is hardly to detect on only one phase CMR Image based on current techniques. Fig 7 shows total 30 different phase CMR Images of slice 12 in one cardiac cycle. The intensity of blood in RV is different with other organs in CMR Images. The blood area looks brighter (that is lighter and whiter) than areas of other organs in CMRI images. This provides a tool to obtain the contour of the blood in 2D RV CMR images and the blood flow can be observed. The blue lines present the top positions of blood in right atrium (RA) in each phase

images. During the RV diastole (Phase 14- Phase29, diastolic phase), the pressure in the right ventricle drops below that in the right atrium, tricuspid valve opens, and the blood that is accumulating in the right atrium is ejected into right ventricle. During the RV systole (Phase 29-Phase 14), the contraction of the heart muscle begins and the pressure in RV rises. When the pressure in right ventricle exceeds in right atrium, the tricuspid valve will closed. Hence, the position of blue line in CMRI images during the phases that tricuspid valve is closed represents the tricuspid valve position. Movie tool can provide a multi-phase view, that's why it is very powerful and helpful. Using movie tool to examine all phases on each slice will help us better "see" heart beats (contracts and expands) and obtain the correct valve position. The contour results were cross-reviewed and verified on ViewForum workstation based on SSFP cine imaging sequences in other different planes (4-chamber plane, and short axis plane) to demonstrate the accuracy and reliability of the results. The segmentation results were also verified by Prof. Geva.

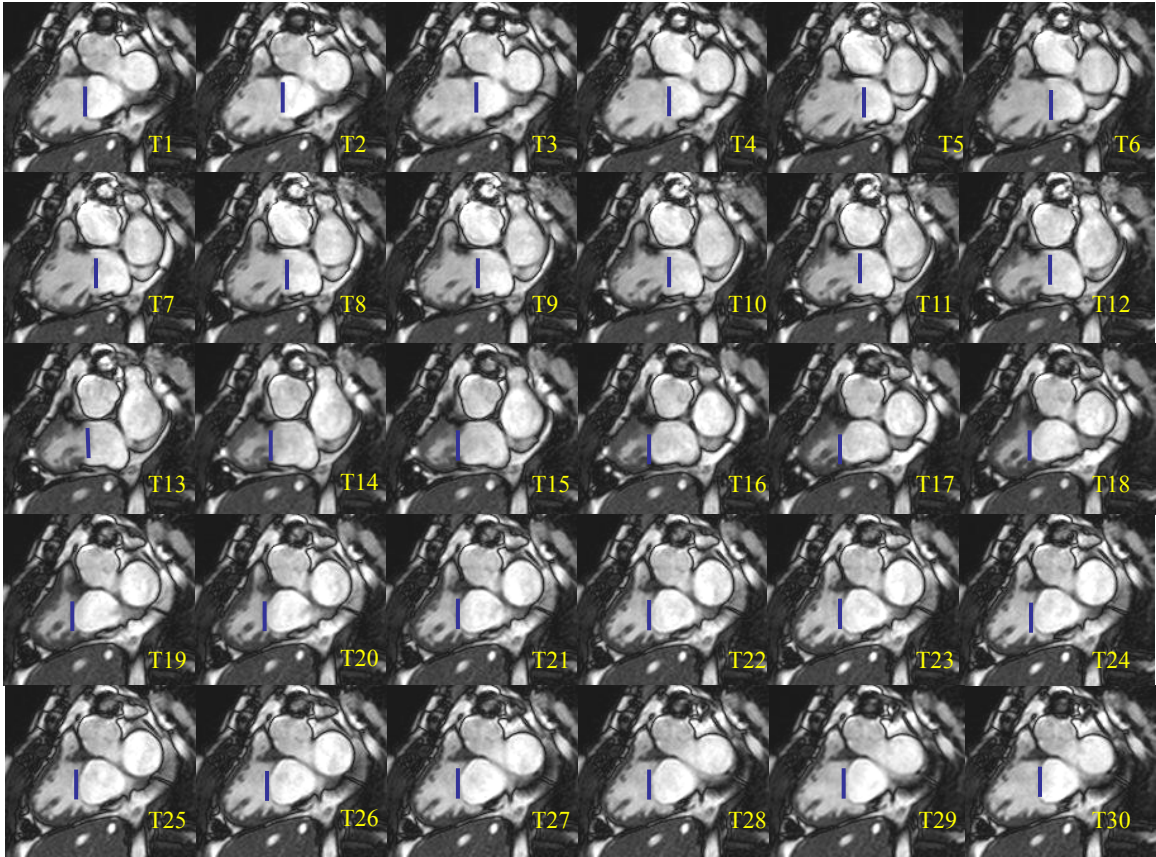


*Fig. 7. CMR Images of slice 12 for all phases (Time 1-Time 30) in a cardiac cycle.*

To edit/redraw the contours, both Trace mode and point mode could be used. The methods are similar with creating the contour, and will remove the section previously detected and insert the new section.

If the contour essentially fits the outline, but needs some overall reshaping, Contour Shape tools list in Table 2 could be chosen to reshape the contour.

<b>Smooth tool</b>	removes small irregularities from the contour
<b>Decurve tool</b>	removes larger curves from the contour.
<b>Make Convex tool</b>	removes all curves from the contour that point inward
<b>Follow Edge tool</b>	detects the edge, using the existing contour as a model

Table. 2. Contour shape tools for contours refine.

## 4.2 Saving the Digital Contour Results

The digital data of RV/LV epicardial/endocardial contours is needed for performing volumetric analysis of ventricular function RV/LV and computational modeling. Windows print screen key is used to take screen shots. Detecting RV/LV epicardial/endocardial contours based on the saved screen shots and saving the corresponding digital data of the contours are performed under MATLAB environment. The details are the following,

### 4.2.1 Using Print Screen Key to Save Contour Results

When finish segmentation of current study image, press the windows Print Screen key (often abbreviated, such as PrtSc), which usually situates in the upper right corner of keyboard, to capture whatever is currently on the screen. Then press **Ctrl+C** to copy the image, click **Start > All Programs > Accessories > Paint** to open the Microsoft Paint, and press **Ctrl+V** to paste the screenshot and save it as Tagged Image File Format (TIFF) type. Fig. 8 shows the image (CMRI (S9P29) with contour results showed on Active Image View window, and Thumbnail View window was hidden), which is presented on the screen, saved by Print Screen key and Microsoft Paint tool. The image is a RGB color image with 1024 x 1280 x 3 array of color pixels, where each color pixel is a triplet corresponding to the red, green, and blue components and the value of the pixel in each component is in the range of [0 255].

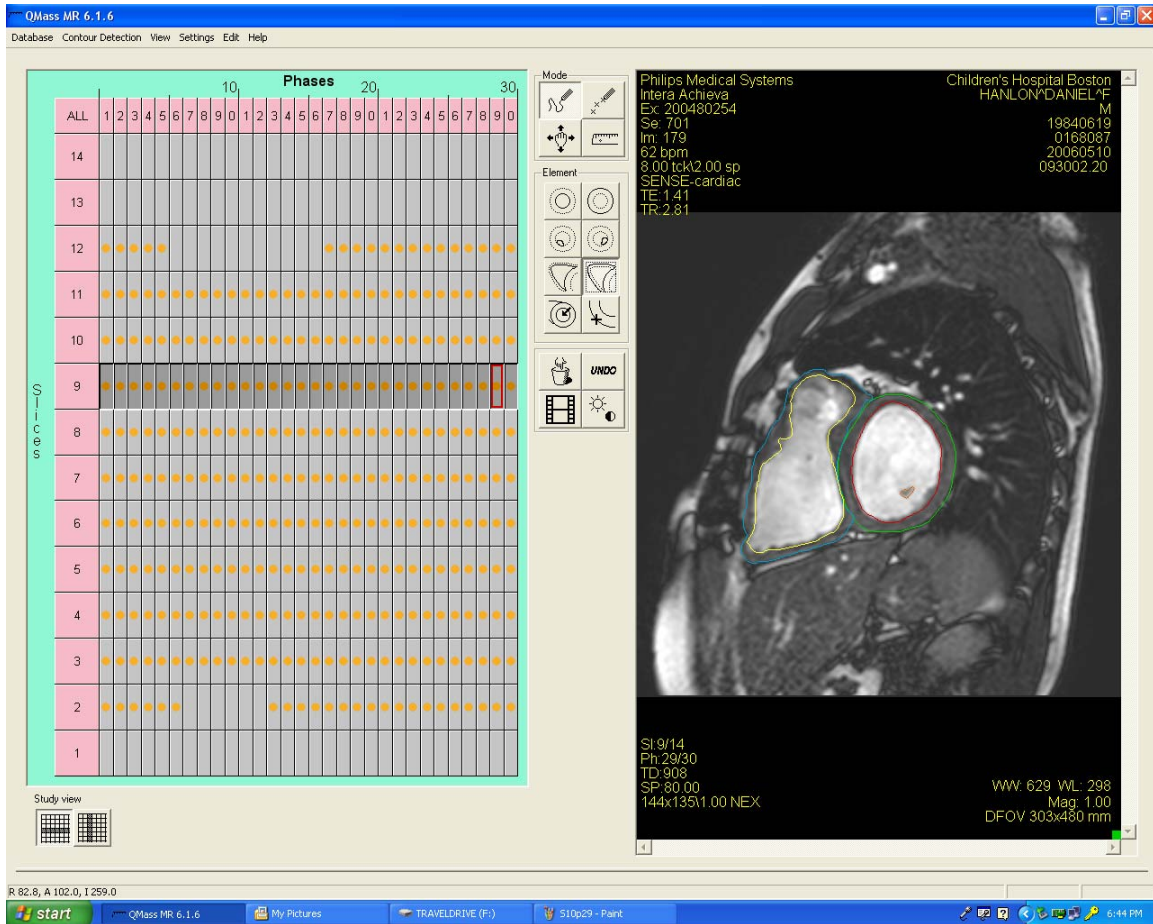


Fig. 8. Image presents on the screen (showing results of S9P29) is saved using Print Screen key.

#### 4.2.2 Obtaining Data of Digital Contours Using MATLAB

The image files (such as Fig. 8), which is saved by the above procedure 4.2.1, will be read by “imread” function in Image Processing Toolbox which is provided by MATLAB and return a 1024 x 1280 x 3 matrix. Fig. 9 (a) shows the selected region of the image (tagged as NL) which is parallel to the original CMRI (tagged as L) with contour results. The size of the NL and L is 538 x 538 and 256 x 256 respectively. NL will be the same as L when shrink it using the proper ratio and nearest-neighbor interpolation. The selected region (NL) will be performed the following image processing.

Actually, the RGB image could be viewed as a “stack” of three gray-scale images. By

conventions, the three gray-scale images were referred to as red, green, and blue component images. For our problem, we only need the information of red component image because that the values of RV/LV epicardial and endocardial contours in red component image are different (Fig. 9 (c)).

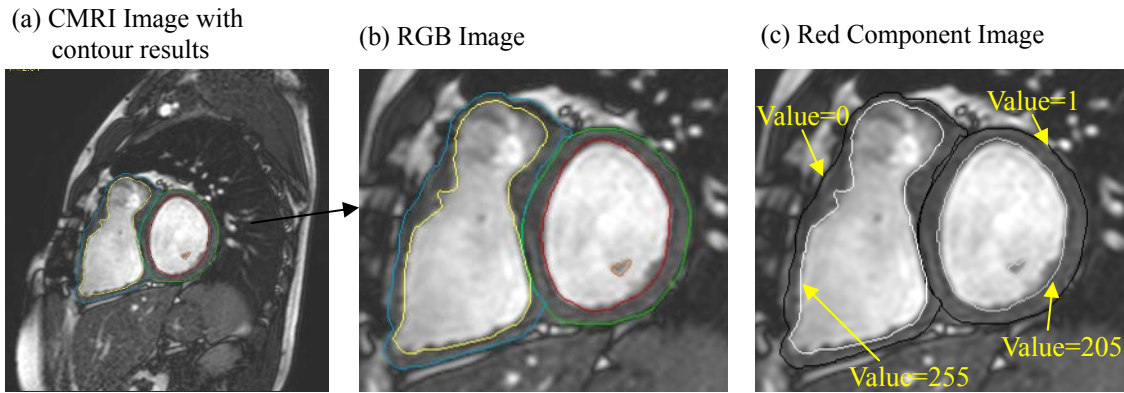


Fig. 9. Images of selected region of S9P29. (a) The region of S9P29 which is parallel to original CMRI Image with contour results; (b) Shows original RGB images of interested (show the region of RV/LV to for better presentation); (c) Red component image showing different value of the 4 different contours.

There are 3 steps to obtain the digital data of RV/LV epicardial/endocardial contour. The following is an example to show how to get the X/Y coordinate values of each point on RV epicardial contour.

### Step 1. Label the image

This step is to generate a new matrix in the same size, in which if the intensity of the pixel is equal to 0, 255, 1, 205, then the value of new matrix will respectively be 1, 2, 3, 4, others will be 0. This procedure will return a matrix with only 5 values (0-4).

## Step 2. Detect the boundary and save the digital contour data

We seek the first point of the line from left lower location of the image as the starting point on the boundary. Each identified pixel has eight directions numbered by 0-7 (Fig. 10) [23]. Since the contour is a closed and connected curve, at least the pixel on one of these directions must also be a new boundary point. Hence each new point in the boundary can be represented by the former point and the direction.

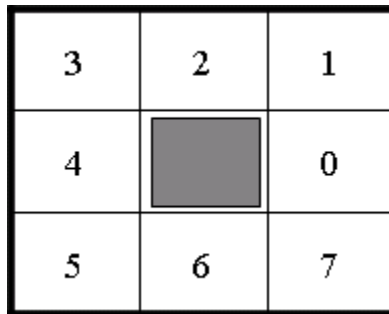


*Fig. 10. Chain code, 0-7 represents 8 directions of the center point [23].*

The following tracking rule was selected to improve the efficiency: Starting from the first point of the boundary, horizontal direction (numbered 0) is chosen as the beginning direction. If the neighbor in horizontal direction is labeled by 1 (that means the point is on the boundary), the current tracking procedure is finish. If not, the direction will be rotated by 45 degree in clockwise direction (the number of direction is added by 1) till to find the first point which is labeled by 1. After these, the X/Y coordinate values of the finding point will be stored; the point in the matrix will be relabeled by 0, and taken as the new boundary point. The current direction will be taken as new direction for the next seeking procedure after rotation by 90 degree in anti-clockwise direction (the number of direction is subtracting by 2). Repeat these steps to find the new point on the boundary until going back to the first point. To save the

storage space, we can only save the X/Y coordinates value of starting point and the directions other than the coordinate values for each new point. To simplify the problem, we saved X/Y coordinate values as the digital contour data. The other contour data can be obtained by repeat the above tracking procedure.

### **Step 3. Restore the contour data to be “real” data**

The digital data we saved in step 2 is the coordinate values of the contours on the images showed on Fig. 9. The data should be shrunk to get the “real” value in the original CMR Images. The resolution of the image is 538 x 538, and the original CMRI image is 256. Hence the shrink ratio should be  $256/538$ .

There are total 420 (14 x 30) images to be saved and performed image processing in Chapter 4.2. These stored digital contour data will be used for 3D-reconstruction, volumetric analysis of RV functions and future computational modeling.



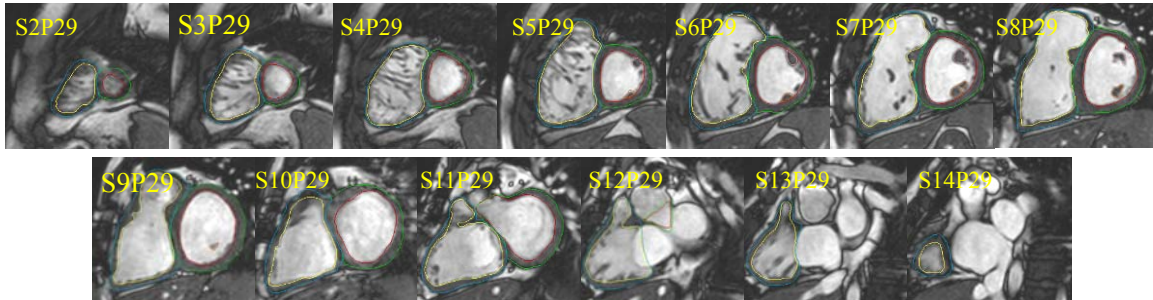
## 5. RESULTS AND ANALYSIS

Once the segmented CMR Images and digital contour data are obtained, we can perform volumetric analysis of RV functions. The results are presented in this chapter.

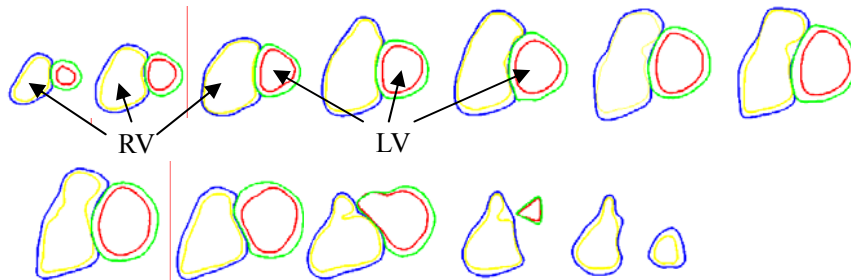
### 5.1 Segmentation Results

Fig 11 shows the segmentation results of CMR Images acquired from the patient at end-diastole phase. Fig 11 (a) gives CMRI with the contour results using QMASS, the job was performed under Dr. Geva and Dr. Powell's guidance in Children's Hospital Boston and the results is also evaluated. Applying the Image processing methods in Chapter 4.2, the digital contour data, which is obtained from Fig. 11 (a), is given by Fig.11 (b).

(a) CMRI Images with the contours, End of Diastole



(b) Segmented contours of RV/LV for Model Construction



*Fig. 11. CMR Images with segmented RV/LV contours (End of Diastole) acquired from a patient showing the RV/LV morphologies*

Fig. 12 presents 3D reconstruction models based on segmented MRI contour results showing RV valve positions with a health human heart sketch (Fig. 12 (a)) and 3D re-constructed RV/LV combination model (Fig. 12 (b)-(d)). Based on our contour results, the 3D geometry of RV/LV model at any phase could be generated. Fig. 12 (d) shows the RV/LV geometry at End of diastole and end of Systole phase. The heart beats (expansion and contraction) could be observed, the heart motions not only in cross-sectional direction but also in axial direction. The variety of volume between end of diastole phase and end of systole phase are calculated in next chapter.

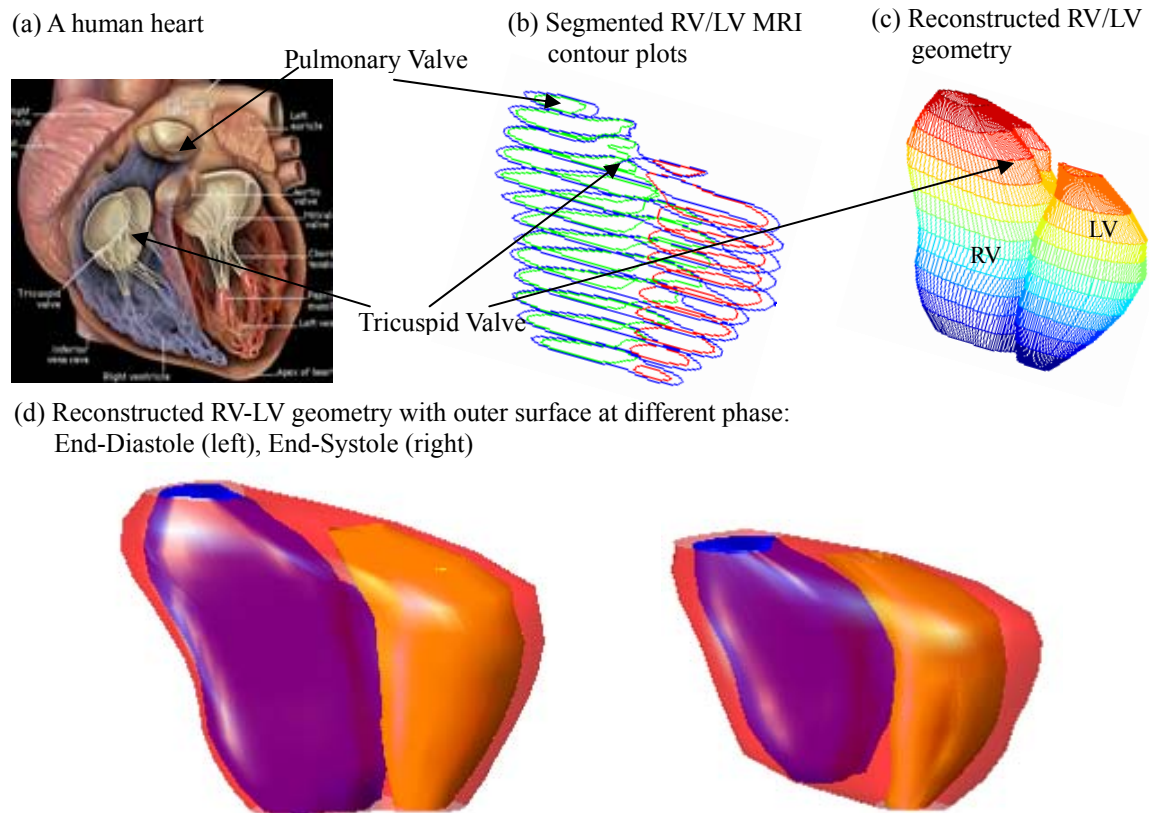


*Fig. 12. Plots showing the 3D-reconstructed model based on segmented result. (a) A health human heart sketch showing left and right ventricles with valve position; (b) Segmented RV/LV MRI contour plots; (c) The re-constructed 3D geometry of the RV/LV combination model; (d) The 3D reconstructed model with outer boundary at End of Diastole (left) and End of Systole (right) showing the heart contraction/ expansion.*

## 5.2 Computing Area and Volume

The area of the RV contour extracted from CMR Image is a very important measure which is essential to RV function analysis. The simplest area measurement is just count the number of pixel inside (and including) the boundary. The other way which is easily computed and only dependent on the contour of object were chosen to calculate the area. The contours were considered as a polygon, and the boundary points  $(x_1, y_1), \dots, (x_n, y_n)$ , where  $n$  is the number of

boundary points, are the vertices of the polygon. Green's theorem says that the area enclosed by a closed curve in the x, y-plane is given by the contour integral,

$$A = \frac{1}{2} \oint (x dy - y dx) \quad (5.1)$$

where the integration is carried out around the closed curve. For discrete segments, equation (5.1) becomes,

$$A = \frac{1}{2} \sum_{i=1}^n [x_i (y_{i+1} - y_i) - y_i (x_{i+1} - x_i)] \quad (5.2)$$

The area of each contour could be calculated by Equation (5.2).

Each slab's volume at one phase can be calculated as the product of its cross-sectional area and thickness based on the above area results. Ventricular volume can be determined by summation of the volumes of all slabs. The process can be repeated for each phase in the cardiac cycle to obtain a continuous time-volume loop RV/LV volume. The curves of RV/LV volume in the whole time-volume loop are presented in Fig. 13, the End of Diastolic volume (EDV) and End of Systole volume (ESV) are also shown on Table 3.

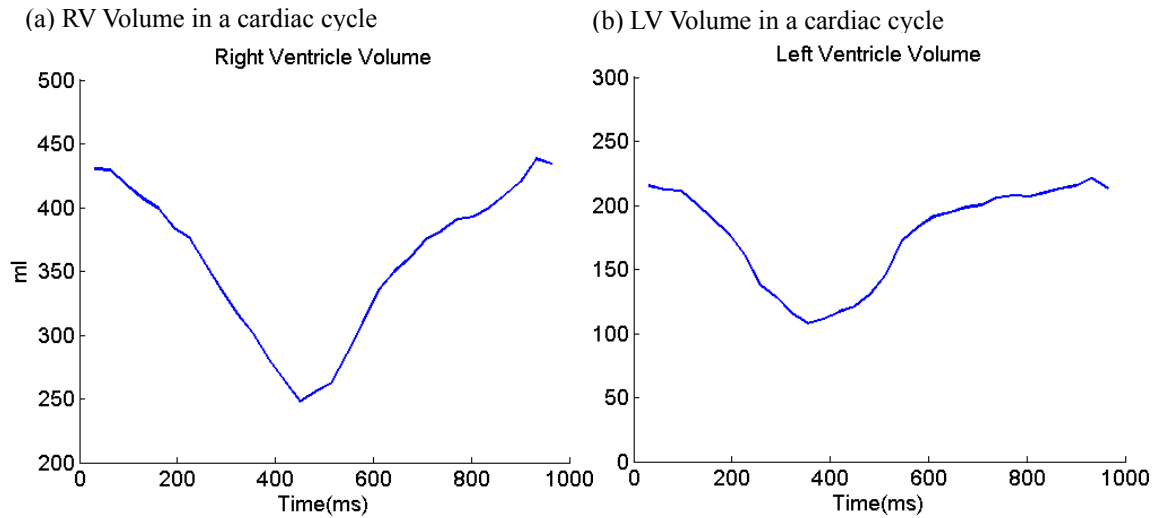


Fig. 13. Patient-specific RV/LV volume curves showing the RV/LV volume variety.

	End of Diastole		End of Systole	
	Phase	Volume (ml)	Phase	Volume (ml)
RV	29	438.4	14	247.5
LV	29	220.9	11	107.8

Table 3. Patient-specific End of Diastolic and Systolic RV/LV volume data.

### 5.3 Ventricle Function Analysis

Based on EDV and ESV results obtained from the above section, stroke volume (SV) and ejection fraction (EF) were calculated by the following definitions,

$$SV = RV \text{ EDV} - RV \text{ ESV} \quad (5.3)$$

$$EF = (RV \text{ EDV} - RV \text{ ESV}) / RV \text{ EDV} \quad (5.4)$$

Right ventricle stroke volume (RV SV) shows the volume of blood in the RV that is pump out and ejection fraction (EF) is the percentage of blood in RV which is pushed out within each beat. Hence RV EF is the measurement showing the heart's pumping ability. RV SV and RV EF are very important measures of RV function. The RV EDV, ESV, SV, and EF were compared with normal value to investigate heart function of this patient. The patient-specific RV volume and comparison results with normal range are summarized in Table 4. Using the minimum normal value as the base, RV EDV, RV ESV, and RV SV value of this patient is 298.5%, 428.1%, and 216% higher, respectively, while RV EF is 30.9% less than maximum normal value. These results provide clear measurement of critical RV function indices, and give initial evidence that this patient has the problem with RV dilation and with heart failure.

	Measured value	Normal range	% of Min_Normal	% of Max Normal
RV EDV (ml)	438.4	110-243	298.5	80.4
RV ESV (ml)	247.5	46-112	438.1	121.0
RV SV (ml)	190.9	60-136	216.7	140.3
RV EF (%)	43.5	47-63	-7.4	-30.9

Table. 4. Summary of RV volume and normal range comparison results.

## **6. FUTURE WORK: MODELING FOR SURGERY OPTIMIZATION**

In this chapter, a patient-specific 3D MRI-based FSI model is introduced. Some baseline results from the RV/LV FSI model for a normal healthy right ventricle are presented. These works were developed by Prof. Tang and Prof. Yang collaborated with Dr. del Nido, and Dr. Geva. A patient-specific RV/LV/Patch combination model will be developed for surgery optimization based on the morphology we obtained in this project in future work. The FSI model makes it possible to combine fluid and structure models to analyze RV function with different patch designs and it can also provide accurate and reliable assessment of RV function prior to surgery. The purpose of computational modeling and simulation is to choose the proper models which include important factors concerning RV function and that can be solved within a reasonable time (e.g., 24 hours) so that surgeons can use the computational analysis to aid and optimize RV remodeling surgery.

### **6.1 3D MRI Based Computational Models**

#### **6.1.1 Solid and Flow Model**

The RV, LV, scar tissue and patch material were all assumed to be hyperelastic, isotropic, nearly-incompressible and homogeneous. The 3D nonlinear modified Mooney-Rivlin (M-R) model was used to describe the material properties of the muscle with parameter values chosen to match experimental data [23, 32, 33]. The flow was assumed to be laminar, Newtonian, viscous and incompressible. The incompressible Navier-Stokes equations with arbitrary Lagrangian-Eulerian (ALE) formulation were used as the governing equations which are suitable for problems with fluid-structure interactions. Pressure conditions were prescribed at the tricuspid (inlet) and pulmonary (outlet) valves [15]. Since RV muscle was treated as passive

material, RV could be inflated properly by modified pressure conditions. No-slip boundary conditions and natural force boundary conditions were specified at all interfaces to couple fluid and structure models together [17, 19]. With all of these, we come to the following FSI model:

$$\rho(\partial\mathbf{u}/\partial t + ((\mathbf{u} - \mathbf{u}_g) \cdot \nabla) \mathbf{u}) = -\nabla p + \mu \nabla^2 \mathbf{u}, \quad (1)$$

$$\nabla \cdot \mathbf{u} = 0, \quad (2)$$

$$\mathbf{u}|_{\Gamma} = \partial \mathbf{x} / \partial t, \quad \partial \mathbf{u} / \partial \mathbf{n}|_{\text{inlet, outlet}} = 0, \quad (3)$$

$$p|_{\text{inlet}} = p_{\text{in}}(t), \quad p|_{\text{outlet}} = p_{\text{out}}(t), \quad (4)$$

$$\rho v_{i,tt} = \sigma_{ij,j}, \quad i,j=1,2,3; \text{ sum over } j, \quad (5)$$

$$\varepsilon_{ij} = (v_{i,j} + v_{j,i})/2, \quad i,j=1,2,3, \quad (6)$$

$$\sigma_{ij} \cdot \mathbf{n}_j|_{\text{out\_wall}} = 0, \quad (7)$$

$$\sigma_{ij}^f \cdot \mathbf{n}_j|_{\text{interface}} = \sigma_{ij}^s \cdot \mathbf{n}_j|_{\text{interface}}, \quad (8)$$

where  $\mathbf{u}$  and  $p$  are fluid velocity and pressure,  $\mathbf{u}_g$  is mesh velocity,  $\Gamma$  stands for RV inner wall,  $\mathbf{f}_{\cdot,j}$  stands for derivative of  $f$  with respect to the  $j$ th variable,  $\boldsymbol{\sigma}$  is stress tensor (superscripts indicate different materials).

The strain energy function for M-R model is given by [23, 32, 33],

$$W = c_1 (I_1 - 3) + c_2 (I_2 - 3) + D_1 [\exp(D_2 (I_1 - 3)) - 1], \quad (9)$$

$$I_1 = \Sigma C_{ii}, \quad I_2 = \frac{1}{2} [I_1^2 - C_{ij}C_{ij}], \quad (10)$$

where  $I_1$  and  $I_2$  are the first and second strain invariants,  $C = [C_{ij}] = X^T X$  is the right Cauchy-Green deformation tensor,  $X = [X_{ij}] = [\partial x_i / \partial a_j]$ ,  $(x_i)$  is current position,  $(a_i)$  is original position,  $c_i$  and  $D_i$  are material parameters chosen to match experimental measurements [11, 23]. The 3D stress/strain relations can be obtained by finding various partial derivatives of the strain energy function with respect to proper variables (strain or stretch components). In particular, setting material density  $\rho = 1 \text{ g} \cdot \text{cm}^{-3}$  and assuming,



$$\lambda_1 \lambda_2 \lambda_3 = 1, \lambda_2 = \lambda_3, \lambda = \lambda_1, \quad (11)$$

where  $\lambda_1$ ,  $\lambda_2$  and  $\lambda_3$  are stretch ratios in the (x,y,z) directions respectively, the uni-axial stress/stretch relation for an isotropic material is obtained from (9),

$$\sigma = \partial W / \partial \lambda = c_1 [2\lambda - 2\lambda^{-2}] + c_2 [2 - 2\lambda^{-3}] + D_1 D_2 [2\lambda - 2\lambda^{-2}] \exp [D_2 (\lambda^2 + 2\lambda^{-1} - 3)]. \quad (12)$$

The parameter values and stress-stretch curves for the baseline model are given by Fig. 14.

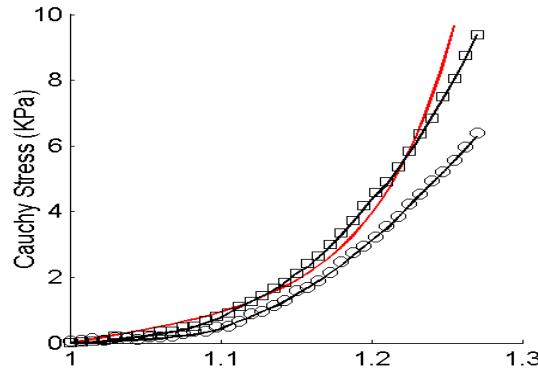
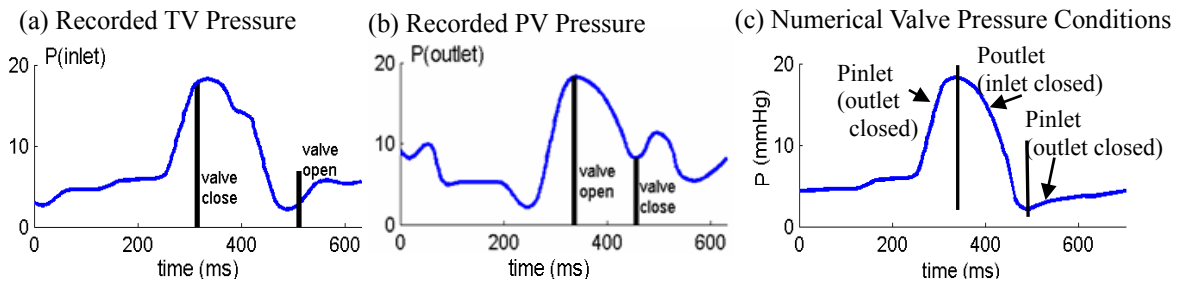


Fig. 14. Experimental data for RV material properties and the stress-stretch curve derived from the Mooney-Rivlin model with parameters selected to fit experimental data. Parameter values used for the MR model:  $c_1 = 3600 \text{ dyn/cm}^2$ ,  $D_1 = 818 \text{ dyn/cm}^2$ ,  $c_2 = 0$ ,  $D_2 = 12$  [11].

For this passive FSI model for normal RV, we start our simulation cycle when RV has its smallest volume (end of systole) corresponding to the minimal inlet pressure ( $t=480 \text{ ms}$ , Fig. 15(c)). As the inlet pressure increases (inlet is kept open), blood flows into RV and its volume increases. When RV reaches its maximal volume, the tricuspid valve closes and the pulmonary valves opens up. Blood is ejected and RV volume decreases. That completes the cycle. While the mechanism driving the motion is different from the real actively contracting heart, our simulated RV motion, deformation, volume change, ejection fraction and fluid flow can provide results matching patient-specific data with properly-adjusted material parameters and

flow-pressure boundary conditions. The recorded and imposed numerical pressure conditions are given in Fig. 15 [15]. To simplify the computational model, the cardiac cycle is split into two phases: a) The filling phase: when blood flows into RV, the inlet is kept open and the outlet is closed; b) The ejection phase: when blood is ejected out of RV, the outlet is kept open and the inlet is closed. When the inlet or outlet are closed, flow velocity is set to zero at the valves and pressure is left unspecified (only one of the two conditions could be specified, or the system become over-determined).



*Fig. 15. Recorded and prescribed pressure conditions at the tricuspid (inlet) valve (TV) and pulmonary (outlet) valve (PV) [15]. Prescribed numerical pressure conditions and valve close/open times were modified from the recorded data so that pressure conditions were as consistent with the recorded data as possible. The vertical bars in (c) indicate valve open/close switch time.*

For simplicity, LV was included as a structure-only model with the same material parameter values used for RV tissues. Blood flow in the LV was not included to reduce the size of the computational code and total CPU time. The inclusion of LV is important to obtain the correct RV motion and deformation. A recorded LV pressure was specified inside the LV so that the LV can expand and contract properly.

### **6.1.2 Solution Procedures**

The computational mesh and finite element model were generated under ADINA computing environment based on RV/LV geometries, and valve locations. The complete LV/RV FSI model was solved by a commercial finite-element package ADINA (ADINA R & D, Inc., Watertown, MA, USA), which has been tested by hundreds of real-life applications and has been used by Tang in the last several years [25-34], to obtain full 3D flow, deformation and stress-strain solutions using unstructured finite elements and the Newton-Raphson iteration method. More details for the solution methods can be found in [2, 3].

### **6.2 Baseline Results from the RV/LV FSI Model for a Normal Healthy RV**

Preliminary results from our baseline RV/LV FSI model based on morphology obtained from a healthy volunteer are given below to demonstrate the basic features of the solutions. While the entire 3D solution data (which includes time-dependent 3D fluid velocity, pressure, RV stress/strain tensor distributions) need to be carefully searched to seek and identify critical information which may be useful in surgical planning and surgery optimization, some cut-surfaces were selected for presentation purpose. Fig. 16 shows the position of a cut-surface chosen to present our results.

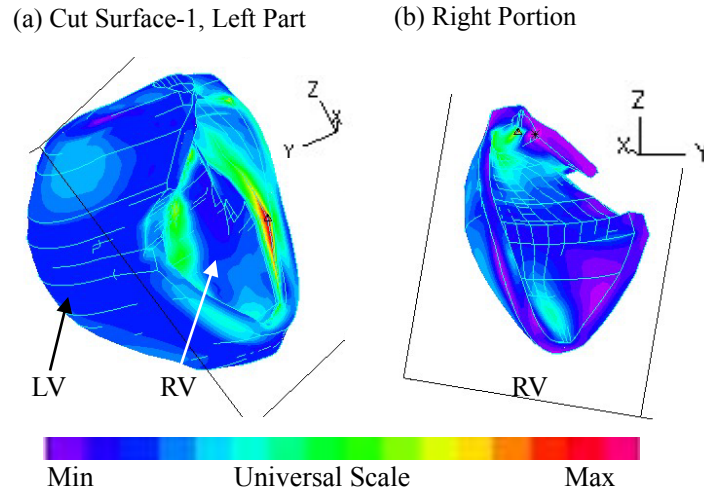


Fig. 16. Position of the cut-surface selected for presentation of 3D results.

Fig. 17 gives some interesting flow patterns in the filling-ejection cycle. At  $t=0.1s$ , the pressure gradient is small, filling is slow. As the pressure gradient increases, flow velocity at the inlet increases which drives the flow in the RV and two vortices are observed ( $t=0.35s$ ). When the inlet closed and outlet just opens ( $t=0.37s$ ), another vortex forms near the inlet and flow starts to eject at the outlet. At  $t=0.39s$ , ejection becomes stronger.

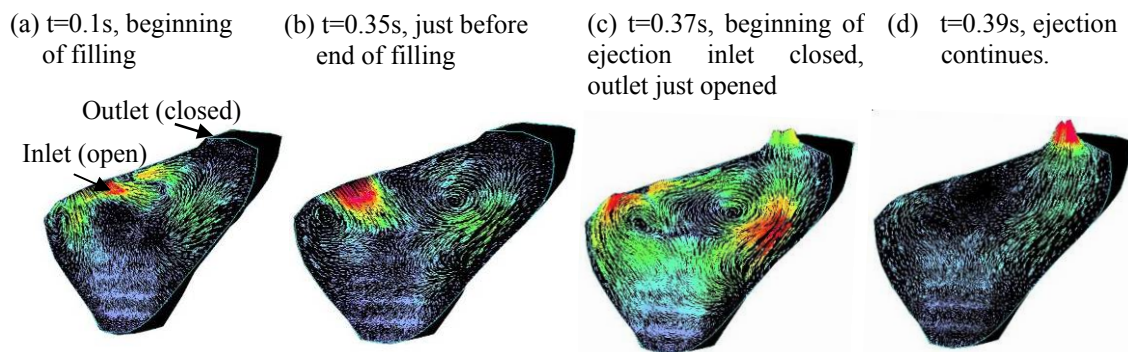
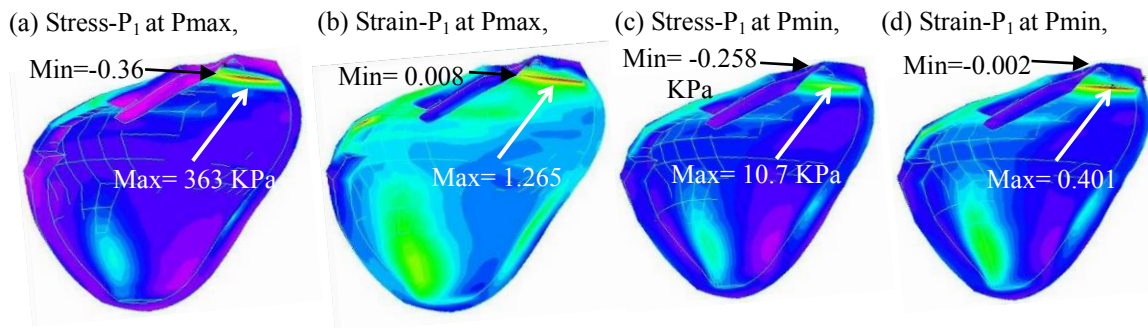


Fig. 17. Velocity plots at different phases showing interesting flow patterns. a) Beginning of the filling phase; b) Flow patterns just before the end of filling phase; c) Beginning of the ejection. The inlet just closed and the outlet valve is open. d) Ejection continues.

Maximal principal stress/strain (Stress-P1 and Strain-P1) distributions on the inner surface of the cut portion corresponding to both maximum and minimum imposed pressure conditions are presented by Fig. 18. The figures are flipped horizontally to have the same position as that in Fig. 16. Maximum stress and strain conditions are found near the outlet (Fig. 18(a-d)) and where surface curvature is large (see Fig. 18(a)). Maximum of the maximum principal stress distribution (Stress-P1) from Fig. 18(a) is 33 times higher than that from Fig. 18(c). Maximum Strain-P1 (maximum principal strain) from Fig. 18(b) is almost 3 times of the maximum Strain-P1 value from Fig. 18(d). The large variation of stress/strain values indicates that there is a large amount of information contained in the stress/strain distributions with the potential to be used for mechanical analysis of patch design and RV function analysis. The locations of maximal stress/strain conditions are mainly associated with large geometry curvatures which indicate the importance of accuracy of MR image technology.



*Fig. 18. Maximal principal stress/strain (Stress-P1 and Strain-P1) distributions on the RV inner surface may provide useful information for mechanical analysis and disease assessment. a) Stress-P1 on the inner surface of RV portion given by Fig. 17; (b) under maximum pressure; b) Strain-P1 on the inner surface of RV under maximum pressure; c)-d) Stress/Strain plots corresponding to minimum pressure condition. Figures were flipped 180° horizontally to have the same view as velocity figures.*

### **6.3 RV Model Development for Surgery Optimization**

A patient-specific RV/LV with scar tissues and/or a patch combination models will be developed to perform analysis of RV flow and structure, stress/strain distributions, and assess RV cardiac function. The surgical, CMR imaging and computational modeling components will be integrated to optimize patch design and RV volume reduction surgery procedures to maximize recovery of RV function. Diagram 1 shows the proposed modeling development and validation plan. The design procedures require four steps: (a) A pre-operation model will be constructed based on the morphology we obtained in this project. This patient is a ToF patient, who's RV does not have a pulmonary valve, the outlet will be kept open with measured pressure condition specified to match measured outflow flow rate data. Patient-specific material parameters will be determined using measured RV pressure and volume data so that computational and CMR volume data reach good agreement; (b) Using the patient-specific model validated by pre-operative data and with guidance from Dr. del Nido, different patch models as indicated in the flowchart will be constructed to make predictions for post-operative outcome. The modified Mooney-Rivlin model was also used for the patch and scar tissue materials with parameters adjusted to reflect the stiffness variations. (c) After the surgery, computational mechanical analysis and predicted RV cardiac function improvements will be provided to Drs. del Nido and Geva for their review after the operation; (d) Post-operative data will be obtained from the same patient six months after the operation to serve as short-term validation of the proposed surgical procedures. The predictive model will be adjusted (morphology, material properties, patch and scar information, pressure conditions) to improve the accuracy of computational predictions.

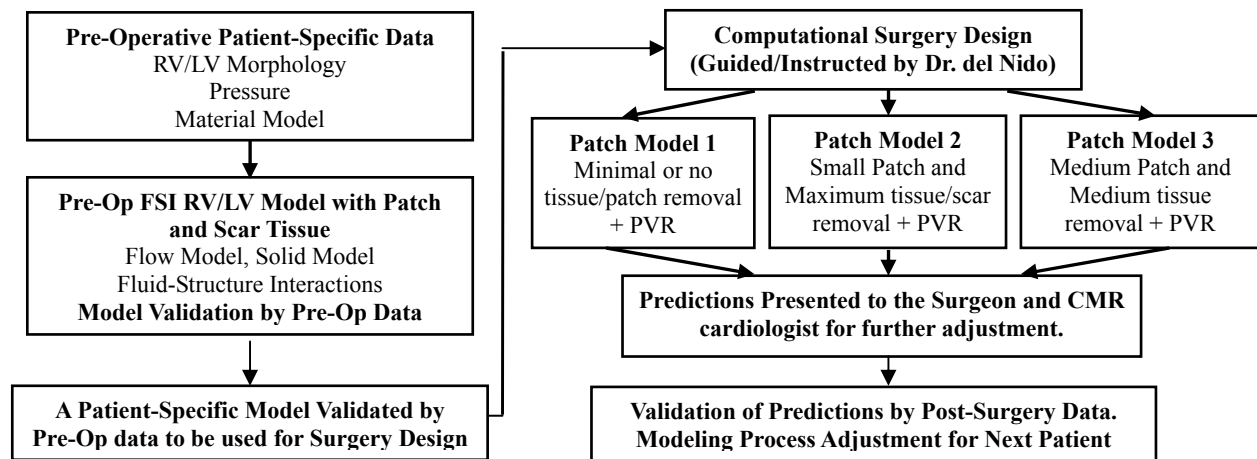


Diagram. 1 A flowchart showing the model development and validation process.

## 7. CONCLUSION AND DISCUSSION

A semi-automatic segmentation process was introduced to obtain patient-specific digital contour data and volumetric analysis of patient-specific right and left ventricles. The project procedure includes the following three components: a) Detecting the patient-specific RV/LV contours on different phase/slice CMR image using QMASS software package in the Department of Cardiology at Children's Hospital Boston. In the clinical setting, only the epicardial/endocardial RV/LV contours are obtained at end-diastole and endocardial RV/LV contours are obtained at end systole (total of 28 slices). In this project, the RV/LV endocardial/epicardial contour results at each phase/slice of the CMR dataset were obtained (total 420 slices,); b) Acquiring digital data of RV/LV contours based on detecting results using DCDHI. The patient-specific 3D reconstructed RV/LV geometries at different phase were obtained based on digital contour data; c) Volumetric analysis: the volumes of RV/LV at each phase were calculated, and the volume curves of RV/LV were presented. The RV stroke volume and ejection fraction were calculated. Comparisons between patient-specific data and normal value for RV EDV, RV ESV, RV SV, and RV EF were presented.

Digitized contours of RV/LV from CMR saved in plain text format with coordinates of all the contour points are needed for building 3D computational models. The RV/LV volume data will be used to determine patient-specific parameter values of material models. Computer-simulated heart motion will be compared with recorded heart motion by 3D reconstructed models. These patient-specific data will improve the accuracy of image-based computational models. Different patch models will be developed to perform patch-design simulations and predict post-operation RV cardiac function.

This project gave me an eye-opening opportunity to perform segmentation of CMR data in



the Department of Cardiology at Children's Hospital Boston and helped me better understand the heart motion in ToF, which is essential for future RV/LV/Patch combination FSI computational model. Communication and collaboration with external and non-mathematician experience will also help me a lot in my future career in the field of applied mathematics.

## REFERENCES

1. Axel L, Biomechanical dynamics of the heart with MRI, *Annu. Rev. Biomed. Eng.*, 2002;4:321-347.
2. Bathe KJ, *Theory and Modeling Guide*, Vol I: ADINA; Vol II: ADINA-F, ADINA R&D, Inc., Watertown, MA, 2002.
3. Bathe K. J, *Finite Element Procedures*. Prentice Hall, 1996.
4. del Nido, PJ. Surgical Management of Right Ventricular Dysfunction Late after Repair of Tetralogy of Fallot: Right Ventricular Remodeling Surgery, *Semin Thorac Cardiovasc Surg Pediatr Card Surg Annu.* 2006:29-34.
5. Furber A, Balzer P, Cavaro-Menard C, Croue A, Da Costa E, Lethimonnier F, Geslin P, Tadei A, Jallet P, Le Jeune JJ. Experimental validation of an automated edge-detection method for a simultaneous determination of the endocardial and epicardial borders in short-axis cardiac MR images: application in normal volunteers. *J Magn Reson Imaging.* 1998;8:1006-1014.
6. Gatzoulis MA, Balaji S, Webber SA, Siu SC, Hokanson JS, Poile C, Rosenthal M, Nakazawa M, Moller JH, Gillette PC, Webb GD, Redington AN. Risk factors for arrhythmia and sudden cardiac death late after repair of tetralogy of Fallot: a multicentre study. *Lancet*, 2000; 356:975-981.
7. Geva T. Introduction: magnetic resonance imaging. *Pediatr Cardiol* 21:3, 2000
8. Geva T, Greil GF, Marshall AC, Landzberg M, Powell AJ. Gadolinium-enhanced 3-dimensional magnetic resonance angiography of pulmonary blood supply in patients with complex pulmonary stenosis or atresia: comparison with x-ray angiography. *Circ.* 2002;106:473-478.
9. Geva T, Sahn DJ, Powell AJ. Magnetic resonance imaging of congenital heart disease in

- adults. *Progress in Pediatr Cardiol* 17: 21, 2003
10. Helbing WA, de Roos A. Optimal imaging in assessment of right ventricular function in tetralogy of Fallot with pulmonary regurgitation. *Am J Cardiol*. 1998;82:1561-1562.
  11. Humphrey J. D., *Cardiovascular Solid Mechanics*, Springer-Verlag, New York, 2002.
  12. Just H, Holubarsch C, Friedburg H. Estimation of left ventricular volume and mass by magnetic resonance imaging: comparison with quantitative biplane angiocardiology. *Cardiovasc Intervent Radiol*. 1987;10:1-4.
  13. Keane J.F., Fyler D.C., Lock J.E. *Nadas' Pediatric Cardiology*, 2nd Edition, Saunders, 2006
  14. Kondo C, Caputo GR, Semelka R, Foster E, Shimakawa A, Higgins CB. Right and left ventricular stroke volume measurements with velocity-encoded cine MR imaging: in vitro and in vivo validation. *AJR Am J Roentgenol*. 1991;157:9-16.
  15. Kuehne T., et al, Magnetic resonance imaging analysis of right ventricular pressure-volume loops, *Circ*. 2004;110:2010-16.
  16. Lee D, Fuisz AR, Fan PH, Hsu TL, Liu CP, Chiang HT. Real-time 3-dimensional echocardiographic evaluation of left ventricular volume: correlation with magnetic resonance imaging--a validation study. *J Am Soc Echocardiogr*. 2001;14:1001-1009.
  17. Mulla N, Simpson P, Sullivan NM, Paridon SM. Determinants of aerobic capacity during exercise following complete repair of tetralogy of Fallot with a transannular patch. *Pediatr Cardiol*. 1997;18:350-356.
  18. Nichols K, Saouaf R, Ababneh AA, Barst RJ, Rosenbaum MS, Groch MW, Shoyeb AH, Bergmann SR. Validation of SPECT equilibrium radionuclide angiographic right ventricular parameters by cardiac magnetic resonance imaging. *J Nucl Cardiol*. 2002;9:153-160.
  19. Nollert G, Fischlein T, Bouterwek S, Bohmer C, Dewald O, Kreuzer E, Welz A, Netz H,

- Klinner W, Reichart B. Long-term results of total repair of tetralogy of Fallot in adulthood: 35 years follow-up in 104 patients corrected at the age of 18 or older. *Thorac Cardiovasc Surg.* 1997;45:178-181.
20. Pini R, Giannazzo G, Di Bari M, Innocenti F, Rega L, Casolo G, Devereux RB. Transthoracic three-dimensional echocardiographic reconstruction of left and right ventricles: in vitro validation and comparison with magnetic resonance imaging. *Am Heart J.* 1997;133:221-229.
21. Powell AJ, Geva T. Blood flow measurement by magnetic resonance imaging in congenital heart disease. *Pediatr Cardiol.* 2000;21:47-58.
22. Rosenthal A. Adults with tetralogy of Fallot--repaired, yes; cured, no. *N Engl J Med,* 1993;329:655-656.
23. Russ J. C., *The Image Processing Handbook*, 2<sup>nd</sup> ed, CRC Press, Inc., Boca Raton, FL, 1995.
24. Sacks M. S., Chuong C. J., 1993, Biaxial mechanical properties of passive right ventricular free wall myocardium, *J Biomech Eng*, 115:202-205.
25. Takayama Y, Costa KD, Covell JW. Contribution of laminar myofiber architecture to load-dependent changes in mechanics of LV myocardium. *Am J Physiol Heart Circ Physiol.* 2002 Apr;282(4):H1510-20.
26. Tang D, Yang C, del Nido PJ, Haber I, Geva T, 3D Image-Based Computational Modeling for Patient-Specific Mechanical Analysis of Human Heart Right Ventricles, *Proceedings of the 2005 International Conference on Mathematics and Engineering Techniques in Medicine and Biological Sciences (METMBS '05)*, 2005:190-196.
27. Tang D, Yang C, Geva T, del Nido PJ, Two-Layer Passive/Active Anisotropic FSI Models with Fiber Orientation: MRI-Based Patient-Specific Modeling of Right Ventricular

- Response to Pulmonary Valve Insertion Surgery, *Journal of Molecular & Cellular Biomechanics*, Vol. 4, No. 3, pp. 159-176, 2007.
28. Tang D, Yang C, Geva T, del Nido PJ, Patient-Specific Virtual Surgery for Right Ventricle Volume Reduction and Patch Design Using MRI-Based 3D FSI RV/LV/Patch Models, **Best paper award**, Proceedings of 2007 IEEE/ICME International Conference on Complex Medical Engineering-CME2007, pp. 158-163, 2007.
  29. Tang D, Yang C, Geva T, del Nido PJ, Patient-Specific MRI-Based 3D FSI RV/LV/Patch Models for Pulmonary Valve Replacement Surgery and Patch Optimization, *J Biomech Eng*, 2008, in press.
  30. Tang D, Yang C, Haber I, Geva T, del Nido PJ, Image-Based RV/LV Combination Structure-Only and FSI Models for Mechanical Analysis of Human Right Ventricle Remodeling Surgery Design, *J Biomech*, 2006;9:S438.
  31. Tang D, Yang C, Huang Y, Ku DN. Wall stress and strain analysis using a 3-D thick-wall model with fluid-structure interactions for blood flow in carotid arteries with stenoses. *Computers and Structures*, 1999;72:341-356.
  32. Tang D, Yang C, Kobayashi S, Ku DN. Steady flow and wall compression in stenotic arteries: a 3-D thick-wall model with fluid-wall interactions. *J. Biomech. Engng.*, 2001;123: 548-557.
  33. Tang D, Yang C, Kobayashi S, Ku DN, Simulating cyclic artery compression using a 3-D unsteady model with fluid-structure interactions, *Computers & Structures*, 2002;80:1651-1665.
  34. Tang D, Yang C, Zheng J, Woodard PK, Sicard GA, Saffitz JE, and Yuan C, 3D MRI-Based Multi-Component FSI Models for Atherosclerotic Plaques a 3-D FSI model, *Annals of*

Biomedical Engineering, 2004;32(7):947-960.

35. Tang D, Yang C, Zheng J, Woodard PK, Saffitz JE, Petruccelli JD, Sicard GA, Yuan C, Local Maximal Stress Hypothesis and Computational Plaque Vulnerability Index for Atherosclerotic Plaque Assessment, *Annals of Biomedical Engineering*, 2005;33(12):1789-1801.
36. Usyk TP, McCulloch AD. Relationship between regional shortening and asynchronous electrical activation in a three-dimensional model of ventricular electromechanics. *J Cardiovasc Electrophysiol*. 2003 Oct; 14(10 Suppl):S196-202.
37. Vetter F. J. and McCulloch A. D., 2000, Three-dimensional stress and strain in passive rabbit left ventricle: a model study, *Annals of Biomech. Engng*. 28:781-792.
38. Yang C, Tang D, Haber I, Geva T, del Nido PJ, In vivo MRI-Based 3D FSI RV/LV Models for Human Right Ventricle and Patch Design for Potential Computer-Aided Surgery Optimization, *Computers & Structures*, 85, 988-997, 2007.